this agreement may be fortuitous. An alternative model, based on the product of e^- and h^+ currents, gives a poor description of the relative intensities but a good description of the peak width for $V_d = 8$ V. The key point is that the maximum in emission at $V_g = V_d/2$ is a clear signature of emission caused by carrier recombination in an ambipolar Schottky barrier transistor.

The optical emission from the nanotube devices was further characterized by measuring its polarization. For this purpose, an IR polarizer was inserted between the sample and the IR camera. Figure 4A presents an example of a polar plot showing the intensity of the IR emission (red dots) as a function of the polarization angle from a device operating with $V_g = 4$ V and $V_d = 8$ V. The carbon nanotube is expected to be a linearly polarized dipole radiation source. When the radiating dipole makes an angle θ with respect to the polarizer analysis axis, the component of the emitted field along the polarizer axis is proportional to cosθ. The transmitted intensity therefore is proportional to $\cos^2\theta$. The green lines in Fig. 4 show this ideal $\cos^2\theta$ dependence. The measured data are in reasonable agreement with the expected behavior of a linearly polarized source. Also shown in Fig. 4B is an SEM image of the device covered with SiO_2 oxide, which shows that the peak in the polarized emission occurs when the polarizer is aligned parallel to the carbon nanotube axis.

Because the band gap in carbon nanotubes is inversely proportional to the tube diameter, one should be able to control the wavelength of the optical emission by using tubes of different diameters. In addition, an aggressive scaling of the gate oxide thickness and the use of an insulator with a high dielectric constant are expected to improve the injection efficiency and emission yield, and reduce the operation voltage. Thus, carbon nanotubes offer great promise as a compact, easy-to-integrate nanoscale source of photons for future photonic and optoelectronic devices.

References and Notes
1. J. Wang, M. S. Gudiksen, X. Duan, Y. Cui, C. M. Lieber, *Science* **293**, 1455 (2001).
2. X. Duan, Y. Huang, Y. Cui, J. Wong, C. M. Lieber, *Nature* **409**, 66 (2001).
3. M. S. Gudiksen, L. J. Lauhon, J. Wong, D. C. Smith, C. M. Lieber, *Nature* **415**, 617 (2002).
4. S. Tans, A. Verscheuren, C. Dekker, *Nature* **393**, 49 (1998).
5. R. Martel, T. Schmidt, H. R. Shea, T. Hertel, Ph. Avouris, *Appl. Phys. Lett.* **73**, 2447 (1998).
6. H. T. Soh *et al.*, *Appl. Phys. Lett.* **75**, 627 (1999).
7. V. Derycke, R. Martel, J. Appenzeller, Ph. Avouris, *Nano Lett.* **1**, 453 (2001).
8. X. Liu, C. Lee, C. Zhou, J. Han, *Appl. Phys. Lett.* **79**, 3329 (2001).
9. A. Bachtold, P Hadley, T. Nakanishi, C. Dekker, *Science* **294**, 1317 (2001).
10. A. M. Rao *et al.*, *Science* **275**, 187 (1997).
11. R. Saito, H. Kataura, in *Carbon Nanotubes: Synthesis, Structure, Properties, and Applications*, M. S. Dresselhaus, G. Dresselhaus, Ph. Avouris, Eds. (Springer-Verlag, Berlin, 2001), pp. 213–247.
12. M. J. O'Connell *et al.*, *Science* **297**, 593 (2002).
13. M. S. Fuhrer *et al.*, *Science* **288**, 494 (2000).
14. M. Freitag, M. Radosavljevic, Y. X. Zhou, A. T. Johnson, W. F. Smith, *Appl. Phys. Lett.* **79**, 3326 (2001).
15. R. Martel *et al.*, *Phys. Rev. Lett.* **87**, 256805 (2001).
16. S. Heinze *et al.*, *Phys. Rev. Lett.* **89**, 106801 (2002).
17. The SWNTs were prepared by laser ablation as described in (*18*). They were used without further treatment and were dispersed in dichloroethane by a short exposure to ultrasound.
18. A. Thess *et al.*, *Science* **273**, 483 (1996).
19. J. Appenzeller *et al.*, *Phys. Rev. Lett.* **89**, 126801 (2002).
20. A. Dodabalapur, H. E. Katz, L. Torsi, R. C. Haddon, *Appl. Phys. Lett.* **68**, 1108 (1996).
21. S. M. Bachilo *et al.*, *Science* **298**, 2361 (2002).
22. A. Hagen, T. Hertel, *Nano Lett.* **3**, 383 (2003).
23. We thank R. Smalley and A. Rinzler for supplying the SWNT sample, J. Appenzeller for helpful discussions, K. K. Chan for device processing, and the referee for valuable suggestions.

The Potential for Earthquake Early Warning in Southern California

Richard M. Allen[1]* and Hiroo Kanamori[2]

Earthquake mitigation efforts in the United States currently use long-term probabilistic hazard assessments and rapid post-earthquake notification to reduce the potential damage of earthquakes. Here we present the seismological design for and demonstrate the feasibility of a short-term hazard warning system. Using data from past earthquakes, we show that our Earthquake Alarm System (ElarmS) could, with current TriNet instrumentation, issue a warning a few to tens of seconds ahead of damaging ground motion. The system uses the frequency content of the P-wave arrival to determine earthquake magnitude, an approach that allows magnitude determination before any damaging ground motion occurs.

Current efforts to mitigate seismic hazard in the United States include long-term (50-year) hazard assessment and rapid post-event notification. Long-term hazard mitigation is facilitated by probabilistic ground-shaking maps (*1*), which estimate the probability of ground motion exceeding some threshold during the next 50 years. Such maps are used in the development of building codes intended to prevent the collapse of buildings during an earthquake. Rapid post-event notification in southern California is provided by TriNet (now part of the California Integrated Seismic Network), a network of about 155 station sites with both high dynamic-range broadband and strong-motion instrumentation (*2, 3*). Rapid notification of earthquake source parameters is issued through a pager system called CUBE (*4*) and over the Internet, within minutes of substantial earthquakes. Peak ground motion observations are also used to generate a map of ground motion distribution ("ShakeMap") within 3 to 5 min of an earthquake (*5*).

Earthquake early warning systems (EWSs) provide a few seconds to tens of seconds of warning of oncoming ground motion, allowing for short-term mitigation. EWSs that estimate the severity of ground shaking and the time till that shaking will commence are in operation in Japan, Mexico, and Taiwan. The most basic system, offering no warning time, issues an alarm when ground shaking at the same location exceeds some threshold. When the earthquake source region is some distance from a populated area or city, seismometers can be deployed between the source and the city to detect any earthquake and transmit a warning electronically, ahead of the more slowly moving ground motion. Mexico City is protected by such a front-detection EWS: Seismometers along the coast detect earthquakes in the Guerrero Gap ~300 km southwest of the city and an alarm is issued, providing ~70 s of warning time (*6, 7*). The Central Weather Bureau of Taiwan also uses a front-detection EWS, which requires an average of 22 s to determine earthquake magnitude and location and thus provides warning for areas greater than ~75 km from the epicenter (*8, 9*).

All these EWSs use observations of peak ground motion to estimate the magnitude of an earthquake, which is the most commonly applied and most accurate method of local magnitude determination. However, this approach does not provide the most rapid magnitude estimate. The first seismic arrival from an earthquake is the P wave, which is usually relatively low-amplitude and causes little damage (Fig. 1). It is followed by the S wave, which usually has a larger amplitude and includes the peak ground motion (Fig. 1),

[1]Department of Geology and Geophysics, University of Wisconsin, Madison, WI 53706, USA. [2]Seismological Laboratory, California Institute of Technology, Pasadena, CA 91125, USA.

*To whom correspondence should be addressed. E-mail: rallen@geology.wisc.edu

causing most of the damage to buildings in an earthquake. The warning time can be increased by use of the P-wave arrival to estimate the magnitude of an earthquake. This approach was introduced in Japan in the 1990s; the UrEDAS system uses the P-wave arrival to estimate both the magnitude and location of an earthquake (*10–12*).

The early warning problem in southern California is particularly challenging because the region is dissected by many active faults, including some beneath metropolitan areas (Fig. 2). A previously detailed EWS proposed instrumentation of known faults (*13*) but would have offered no protection against blind thrust faulting such as the Northridge earthquake (*14*). The utility of a front-detection EWS has also been argued (*15*) and applied for aftershocks. After the Loma Prieta earthquake, a front-detection system was used to warn workers of aftershocks as they cleared debris ~100 km from the epicentral region (*16*). Front detection, however, cannot issue any warning in the epicentral region, impeding the effectiveness of such a system when active faults and population centers are in the same location.

Our proposed Earthquake Alarm System (ElarmS) issues a warning based on information determined from the P-wave arrival only, providing the potential to issue a warning before peak ground motion at the epicenter. ElarmS initially determines the location, origin time, and magnitude of an event using the first detected P-wave arrivals. The spatial distribution of anticipated peak ground motion is then determined with attenuation relations. Finally, the warning time is estimated based on the origin time and travel time curves for S waves. Here, we focus on the determination of event magnitude using P-wave arrivals, as we use relatively standard procedures for the other components of ElarmS.

To develop and test the concept of ElarmS, waveform data were gathered for a large number of southern California earthquakes recorded by two or more broadband seismometers within 100 km of the epicenter. The event set consisted of 53 earthquakes. It included all earthquakes with magnitude ≥5.0 since 1995, plus the Northridge, Hector Mine, and Landers earthquakes with magnitudes 6.7, 7.1, and 7.3, respectively (table S1). In addition, two events were selected at random with magnitudes 3.0 to 4.9 (events were binned in 0.1-magnitude-unit bins).

We estimated the magnitude of an earthquake from the frequency content of the P-wave arrival, using an approach similar to that used in Japan (*12*). Small-magnitude events are the result of slip over a small patch of fault and result in the radiation of relatively high-frequency energy compared to larger magnitude events, which rupture large patch-es and radiate lower frequency energy. Therefore, a measurement of the predominant period of a seismic waveform in the few seconds after the P-wave arrival onset can constrain the magnitude. The predominant period is determined continually in real time from the vertical component of the velocity sensor at each station and is defined with the recursive relation

$$T_i^p = 2\pi \sqrt{X_i/D_i} \qquad (1)$$

where

$$X_i = \alpha X_{i-1} + x_i^2 \qquad (2)$$

$$D_i = \alpha D_{i-1} + (dx/dt)_i^2 \qquad (3)$$

T_i^p is the predominant period at time *i*, x_i is the recorded ground velocity, X_i is the smoothed ground velocity squared, D_i is the smoothed velocity derivative squared, and α is a smooth-

ing constant (*17*). The higher frequency content of smaller magnitude earthquakes is measurable within a shorter time period after the P-wave arrival than the low-frequency energy of larger events. Correspondingly, the magnitude of smaller events can be determined more rapidly than that of larger events. This also means that the magnitude estimate after 1 s is a minimum estimate and that once 2, 3, and 4 s of data are available, the magnitude estimate may increase.

Two linear relations between T_{max}^p and magnitude were used (Fig. 3). For smaller earthquakes (magnitudes 3.0 to 5.0), broadband data low-pass filtered at 10 Hz were used and a good magnitude estimate was possible given just 1 s of data. With 2 s of data the magnitude error reduced slightly, but additional data did not improve the estimate. Using our T_{max}^p observations from the broad-

Time (seconds)
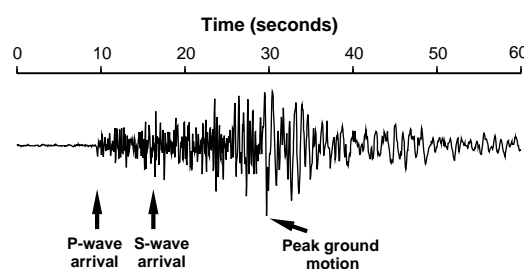
Fig. 1. Typical seismic waveform for a local earthquake. This trace of horizontal ground motion was recorded 50 km from the epicenter of a magnitude 3.9 earthquake in southern California. Indicated are the P-wave and S-wave arrival times and the peak ground motion, which is required to determine local magnitude.
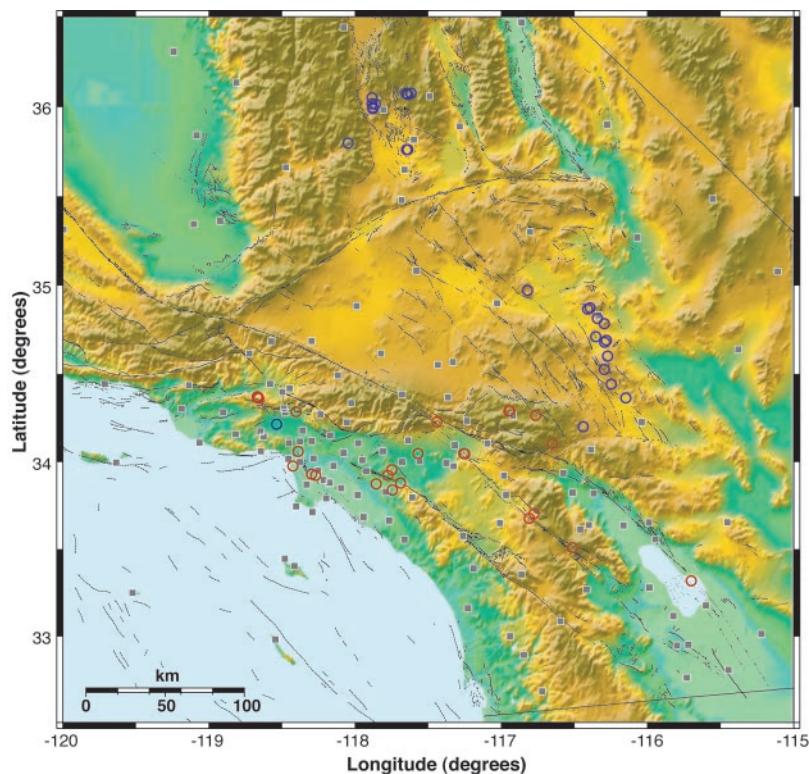
Fig. 2. Tectonic map of southern California showing topography (color scale), mapped fault distribution (thin black lines), locations of the TriNet stations with the necessary real-time capabilities to implement ElarmS (gray squares), and epicenters of the 53 earthquakes used in this study (blue and red circles). The 28 earthquakes used to demonstrate the performance of ElarmS as a function of time are shown in red.

band waveforms after 2 s and minimizing the average absolute deviation, we determined the relation

$$m_l = 6.3\log(T^p_{max}) + 7.1 \qquad (4)$$

to estimate the magnitude of low-magnitude earthquakes (m_l), with an average absolute deviation of 0.3 magnitude units. For larger magnitude events (magnitude >4.5), better estimates are possible with the application of a 3-Hz low-pass filter. The best estimates of magnitude require 4 s of data, although minimum-magnitude estimates can be made as soon as 1, 2, and 3 s after the P-wave arrival. The best-fit high-magnitude (m_h) relation is

$$m_h = 7.0\log(T^p_{max}) + 5.9 \qquad (5)$$

with an average absolute deviation of 0.67 magnitude units.

ElarmS uses both m_l and m_h to produce the best estimate of magnitude. Initially, 1 s after a station triggers, m_l is calculated from T^p_{max}. The estimate is updated when 2 s of data are available. Station-magnitude estimates (one from each triggered station) are averaged to provide an event-magnitude estimate. If the event-magnitude estimate becomes greater than 4.0, then m_h is also calculated and the event-magnitude estimate is the average of both m_l and m_h from each triggered station. The accuracy of the magnitude estimate increases with the number of stations reporting a T^p_{max} observation (Fig. 3). With a single T^p_{max} from the closest station, the average absolute error in the magnitude estimate is ±0.70, but when the closest 10 stations are used, the average error drops to ±0.35 (Fig. 4A and fig. S1).

Another key element of an early warning system is its ability to process the necessary information in the shortest possible time, in order to issue an initial warning as soon as possible, and then to update that warning as more data become available. Our approach to magnitude determination provides the first magnitude estimate within 1 s of the first P-wave trigger. Depending on the S-minus-P time, which will vary according to the depth of the event and the proximity of the closest station, this estimate may be determined before the S-wave arrival at the epicenter. Thirty km from the epicenter, the magnitude would be available ~8 s before the S-wave arrival, and at 60 km, the magnitude would be available ~16 s before the S-wave arrival.

To demonstrate the time history of the ElarmS magnitude estimate and to show how the system could operate today given the current TriNet station density in the more populated regions of southern California, we used a subset of 28 of our 53 earthquakes (Fig. 2 and table S1). We assessed the timeliness with which the magnitude estimate becomes available by determining the error in the ElarmS magnitude estimate as a function of time (Fig. 4B). The zero time was the S-wave arrival at the epicenter, because it represents the earliest time of damaging ground motion. Of the 28 events, a magnitude estimate was available for 12 at the time of the S-wave arrival at the epicenter. The magnitude estimates were variable during the time window −1 to +2 s, but then became stable (Fig. 4B and fig. S2). The average absolute error in the magnitude estimate steadily dropped from 0.41 to 0.26 magnitude units in the period from 2 to 5 s after the S-wave arrival at the epicenter (Fig. 4B).

This subset of events did not include the three largest magnitude events (Landers, Northridge, and Hector Mine), because none of these were sampled by the dense station network now available in populated regions of southern California. Although these events require an additional 2 s for the best magnitude estimates, the peak ground motion for such large-magnitude events can occur tens of seconds after the S-wave arrival. In the case of Northridge, peak ground motion at the closest station (32 km from the epicenter) occurred 5 s after the S-wave arrival; the two broadband waveforms for Landers (at 62 and 65 km) showed a 10- to 15-s delay between the S-wave arrival and peak ground motion.
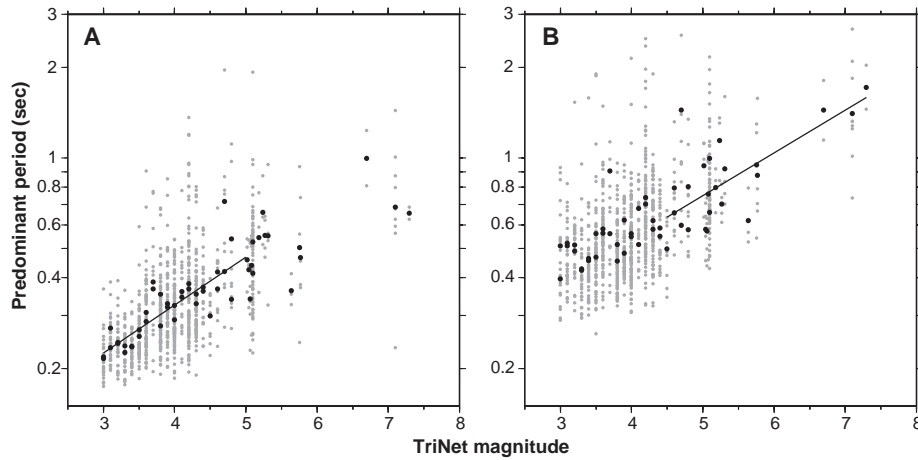
Fig. 3. Relation between predominant period and magnitude. The predominant period is measured on the vertical component of a broadband velocity sensor. (**A**) Maximum predominant period observed within 2 s of the P-wave arrival low-pass filtered at 10 Hz versus TriNet magnitude for individual stations (gray dots) and event averages (black dots) for all 53 events. The black line is the best fit (least absolute deviation of event averages) for data from magnitude 3.0 to 5.0 events. (**B**) The maximum predominant period within 4 s of the P-wave arrival on the same data stream low-pass filtered at 3 Hz. The black line is the best fit to event averages for earthquakes with magnitude between 5.0 and 7.3. Observations of the predominant period at single stations show noticeable scatter (gray dots); once data from several stations are averaged, the scatter reduces substantially (black dots).

Fig. 4. (**A**) Error in ElarmS magnitude estimate as a function of the number of stations reporting. Each histogram shows the frequency distribution of the magnitude error given the number of reporting stations. The total number of event-magnitude estimates included and the average absolute error are shown for each histogram. (**B**) Error in ElarmS magnitude estimate as a function of time with respect to the S-wave arrival at the epicenter (−1 s is 1 s before the S-wave arrival). Magnitude estimates are available for 2, 12, and 19 events (of the 28-event data set) at −1, 0, and 1 s with average errors of 0.61, 0.52, and 0.56 magnitude units, respectively (figs. S1 and S2).
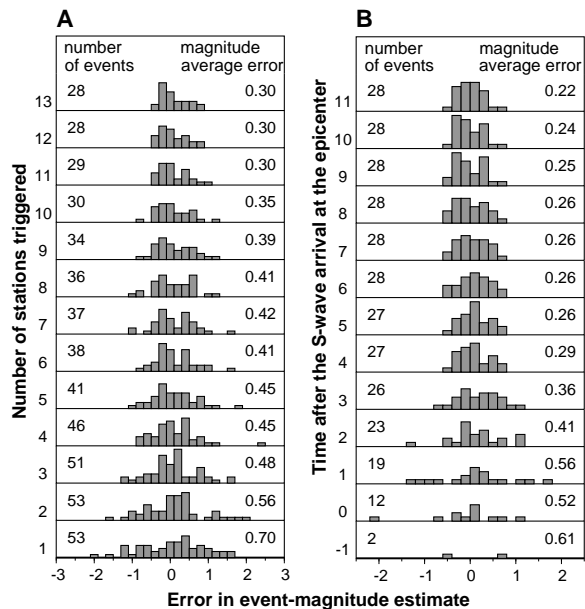
The tests of ElarmS presented here use data from past earthquakes. In a real-time implementation of ElarmS, the total processing time would be increased by data transmission times. Current TriNet stations are able to perform waveform processing on site. Because only parameter information is transmitted to central processing, transit time is reduced, allowing the processing of station information at the central site 1 s behind real time. The delay in transmitting the warning would be dependent on the technology used but could be reduced to less than 1 s. It is therefore conceivable to issue a ground-motion warning across southern California within 2 s of the times shown in Fig. 4B.

In conclusion, the implementation of ElarmS could provide a few to tens of seconds of warning to areas that may suffer structural damage in an earthquake. Buildings up to 60 km from the epicenter were red-tagged for demolition after the magnitude 6.7 Northridge earthquake. In a repeat event, occupants of buildings ~60 km from the epicenter could receive ~20 s of warning before peak ground motion. In a larger magnitude earthquake, the area damaged could be larger and even more warning time would be available to those further from the epicenter. For example, in the 1999 magnitude 7.6 Chi-Chi earthquake in Taiwan, many buildings were moderately damaged in the capital city of Taipei 145 km from the epicenter (18). With the ElarmS approach, there could be ~40 s of warning at a distance of 145 km.

The potential uses of a few to tens of seconds of warning span both personal and institutional preservation. Personal protective measures that could be undertaken at home and in the workplace include getting under desks and moving away from dangerous chemicals and machinery. During the response to a major earthquake, ElarmS could provide warning to rescue and clean-up personnel as they work on unstable debris. Institutional uses of short-term warnings include automated mass-transportation systems that can use a few seconds to slow and stop trains, abort airplane landings, and prevent additional cars from entering the freeway. Industry can shut down, or initiate the shutdown process of, sensitive equipment before peak ground motion arrives, preventing cascading failures. In addition to these immediate uses, the development of an early warning system will lead to the development of infrastructure that can use the information. For example, engineering companies in Japan are developing buildings with active response systems: The buildings can change their mechanical properties within a few seconds to better withstand ground motion (19).

References and Notes
1. A. Frankel et al., "National seismic hazard maps," *Tech. Report No. Open-File Report 96-532* (U.S. Geological Survey, 1996).
2. H. Kanamori, E. Hauksson, T. Heaton, *Nature* **390**, 461 (1997).
3. E. Hauksson et al., *Seismol. Res. Lett.* **72**, 690 (2001).
4. H. Kanamori, E. Hauksson, T. Heaton, *Eos* **72**, 564 (1991).
5. D. J. Wald et al., *Earthquake Spectra* **15**, 537 (1999).
6. J. M. Espinosa Aranda et al., *Seismol. Res. Lett.* **66**, 42 (1995).
7. J. Anderson et al., *Seismol. Res. Lett.* **66**, 11 (1995).
8. Y. M. Wu, T. C. Shin, Y. B. Tsai, *Bull. Seismol. Soc. Am.* **88**, 1254 (1998).
9. Y.-M. Wu, T.-L. Teng, *Bull. Seismol. Soc. Am.* **92**, 2008 (2002).
10. Y. Nakamura, B. E. Tucker, *Earthquakes Volcanoes* **20**, 140 (1988).
11. Y. Nakamura, B. E. Tucker, *Calif. Geol.*, **41**, 33 (1988).
12. Y. Nakamura, *Proc. World Conf. Earthquake Eng.* **VII**, 673 (1988).
13. N. M. Toksoz, A. M. Dainty, J. T. Bullitt, *PAGEOPH* **133**, 475 (1990).
14. L. Jones et al., *Science*, **266**, 389 (1994).
15. T. H. Heaton, *Science* **228**, 987 (1985).
16. W. H. Bakun, F. G. Fischer, E. G. Jensen, J. Vanschaack, *Bull. Seismol. Soc. Am.* **84**, 359 (1994).
17. Materials and methods are available as supporting material on *Science* Online.
18. Y. B. Tsai, T. M. Yu, H. L. Chao, C. P. Lee, *Bull. Seismol. Soc. Am.* **91**, 1298 (2001).
19. G. W. Housner, L. A. Bergman, T. K. Caughey, A. G. Chassiakos, R. O. Claus, S.F. Masri, R. E. Skelton, T. T. Soong, B. F. Spencer, J. T. P. Yao, *J. Eng. Mech. ASCE* **123**, 897 (1997).
20. We thank Y. Nakamura of Systems and Data Research Company, Japan, for discussions regarding UrEDAS, the Japanese earthquake early warning system; E. Hauksson and P. Small, both at the California Institute of Technology (Caltech), for their participation in discussions of the technical capabilities of TriNet; and two anonymous reviewers for their comments on this manuscript. Supported by the Seismological Laboratory at Caltech and the Graduate School of the University of Wisconsin–Madison.

Iron Partitioning in Earth's Mantle: Toward a Deep Lower Mantle Discontinuity

James Badro,[1] Guillaume Fiquet,[1] François Guyot,[1] Jean-Pascal Rueff,[2] Viktor V. Struzhkin,[3] György Vankó,[4] Giulio Monaco[4]

We measured the spin state of iron in ferropericlase $(Mg_{0.83}Fe_{0.17})O$ at high pressure and found a high-spin to low-spin transition occurring in the 60- to 70-gigapascal pressure range, corresponding to depths of 2000 kilometers in Earth's lower mantle. This transition implies that the partition coefficient of iron between ferropericlase and magnesium silicate perovskite, the two main constituents of the lower mantle, may increase by several orders of magnitude, depleting the perovskite phase of its iron. The lower mantle may then be composed of two different layers. The upper layer would consist of a phase mixture with about equal partitioning of iron between magnesium silicate perovskite and ferropericlase, whereas the lower layer would consist of almost iron-free perovskite and iron-rich ferropericlase. This stratification is likely to have profound implications for the transport properties of Earth's lowermost mantle.

Recent seismic observations (1) suggest that compositionally distinct domains exist in Earth's lower mantle, with a boundary located between 1700- and 2300-km depths. For these observations to be interpretable, the chemical and physical properties of the dominant phases in the lower mantle—namely $(Mg,Fe)SiO_3$ magnesium silicate perovskite (hereafter called

perovskite) and $(Mg,Fe)O$ ferropericlase—must be determined at the pressure and temperature conditions of the deep mantle. In turn, these data can be fed into geochemical and geodynamical models (2, 3). The thermodynamic stability of perovskite at the pressure and temperature conditions of the lower mantle (4–9) indicates that it is stable to at least 2300 km depth (9). On the other hand, more subtle effects, driven by the chemistry of iron in the lower mantle, can affect the iron content in perovskite and ferropericlase; that is, they can affect the partition coefficient of iron between the two compounds. It has been suggested theoretically (10, 11) that iron in ferropericlase undergoes a high-spin (HS) to low-spin (LS) transition in the pressure domain of the lower mantle, and that iron in perovskite remains in

[1]Laboratoire de Minéralogie–Cristallographie de Paris, Université Paris VI, Université Paris 7, CNRS, IPGP, 4 place Jussieu, F-75252 Paris Cedex 05, France. [2]Laboratoire de Chimie Physique–Matière et Rayonnement (UMR 7614), Université Paris VI, 11 rue Pierre et Marie Curie, F-75231 Paris Cedex 05, France. [3]Geophysical Laboratory, Carnegie Institution of Washington, 5251 Broad Branch Road, N.W., Washington, DC 20015, USA. [4]European Synchrotron Radiation Facility (ESRF), B.P. 220, F-38043 Grenoble Cedex, France.